JAAS

PAPER

View Article Online
View Journal | View Issue

Cite this: *J. Anal. At. Spectrom.*, 2024, **39**, 2565

Optimizing SEM-EDX for fast, high-quality and non-destructive elemental analysis of glass†

Paul C. Guyett, *[ab] David Chew, [ab] Vitor Azevedo, [a] Lucy C. Blennerhassett,[ab] Carolina Rosca ‡[a] and Emma Tomlinson[ab]

Advancements in scanning electron microscopy and energy dispersive X-ray analysis (SEM-EDX) technologies have reached the point where rapid, fully quantitative, non-destructive and high-resolution acquisition of effectively all major element chemical information from polished sample material is possible. Here, we discuss optimisation parameters and demonstrate the data quality that can be achieved for SEM-EDX analysis of magmatic glass samples; glass represents a particular challenge due its lack of stoichiometry and potential for beam-induced element mobilisation. We test our approach through analysis of reference materials and demonstrate the advantages of SEM-EDX for several volcanic glasses that were previously investigated with electron probe micro-analysis (EPMA). SEM-EDX analysis is typically undertaken at a much lower beam current than EPMA, allowing for non-destructive analysis of geologic material that are sensitive to a higher beam current, such as sodium-rich glass. With careful instrument set-up, robust standardisation, and optimal experiment parameters, SEM-EDX analysis can achieve major and minor element data comparable with that collected *via* EPMA, with the exception of low abundance elements (those below 0.2 wt%). In addition, SEM-EDX analysis typically uses a smaller beam diameter and so permits analysis of smaller features than EPMA. Our results show that this technique can be potentially used as a quantitative tool on a wide range of geological materials with faster analysis, improved spatial resolution and cost advantages making it a complementary or alternative analytical method to EPMA.

Received 7th June 2024
Accepted 29th August 2024

DOI: 10.1039/d4ja00212a

rsc.li/jaas

1. Introduction

SEM-EDX is a powerful technique for rapid, quantitative, non-destructive, and high-resolution acquisition of effectively all major element chemical information. For several reasons, SEM-EDX has not gained acceptance for quantitative analysis compared to EPMA.[1] In this study we apply SEM-EDX analysis to glass – a matrix that is non-stoichiometric and potentially is at risk of beam-induced volatile loss. If SEM-EDX can collect precise and accurate analysis on a challenging matrix such as glass, then it follows that analysis of any polished material matrix for major and minor elements should be possible. Microbeam major element characterisation has been shown to be a very powerful approach to investigate the geological and archaeological genesis and origin of glass, as well as having forensic applications. As some glass samples are often either small (*e.g.* tephra down to the micron scale), spatially heterogenous or valuable, *in situ* quantitative analysis is required. We define major elements as above 1 wt%, minor elements as between 1 wt% and 0.1 wt% (1000 ppm), and trace elements as below 1000 ppm. We refer to concentrations herein as wt% oxide as this is easier to understand in terms of the composition of geological materials. For geologic materials the major elements typically include Si, Al, Ca, Na, K, Fe, and Mg while the minor elements Mn, Ti, Ni, Cr, P and S are also often measured. Additionally, elements such as Pb and U may be major components of archaeological glass (*e.g.*, ref. 2). In terms of geological analysis, major element geochemical analysis of volcanic glass has been used for tephrostratigraphy and for understanding magma petrogenesis. Analysis of magmatic glasses such as obsidian lavas and volcanic ash can provide information on magmatic differentiation processes and the magma source (*e.g.* ref. 3 and 4). Tephrostratigraphy employs glass-bearing volcanic ash layers as stratigraphic markers in sedimentary, ice core or archaeological settings (*e.g.* ref. 5, 6 and 7). The post-emplacement alteration of magmatic glass can also be investigated (*e.g.* ref. 8 and 9). Determining the provenance of an item of archaeological interest in a non-destructive manner is critically important (*e.g.*, ref. 10 and 11). Non-destructive analysis of glass samples in the field of forensics, where repeat analysis of tiny amounts of samples have been

[a]*Department of Geology, School of Natural Sciences, Trinity College Dublin, Dublin 2, Ireland. E-mail: guyettp@tcd.ie*

[b]*iCRAG, SFI Research Centre for Applied Geosciences, Ireland*

† Electronic supplementary information (ESI) available. See DOI: https://doi.org/10.1039/d4ja00212a

‡ Now at: Spanish National Research Council (CSIC), Andalusian Earth Science Institute (IACT), 18100 Granada, Spain.

recovered, is also of vital importance. Forensic activities can range from analysis of material found at crime scenes[12] to detecting forgeries.[13] Faster analysis, and therefore increased sample throughput, offers advantages for commercial applications such as exploration.

The current method of choice for accurate *in situ* major analysis of glass is wavelength dispersive X-ray spectrometry electron microprobe analysis (WDS-EPMA), which has a typical detection limit of 100 ppm and an accuracy of ±5%.[1] Concentrations in the low ppm range can also be determined for some sample matrices, but this requires exceptional analytical conditions with very high beam currents and long counting times and are only suitable for certain matrices.[14] In addition, WDS detectors can only analyse one element at a time, thus modern WDS-EPMA operate with up to five WDS detectors running simultaneously, which increases the cost of the instrument. Analysis of mobile and volatile elements must be completed first, potentially using different experimental setup, and analysis of more than five elements may require an extended run time of several minutes per analysis. By contrast, SEM-EDX as a non-crystalline material, glass is highly susceptible to beam damage, leading to migration of mobile cations (*e.g.*, Cl, Na, K) (*e.g.*, ref. 15, 16, 17 and 18). Therefore, analysis of glass requires specific analytical conditions, for example low beam current,[16] use of a defocused beam or analysis at cryogenic temperatures.[19]

One of the main alternative analytical methods to WDS-EPMA is scanning electron microscope – energy dispersive X-ray spectroscopy (SEM-EDX or SEM-EDS). This technique is relatively low cost and widely available, but has detection limit of approximately 0.1 wt%.[20] In addition, it is possible to run EDX alongside WDS-EPMA where EDX can collect major elements simultaneously to the WDS-EPMA characterisation of trace element chemistry.[14] In SEM-EDX analysis, all elements are determined simultaneously, therefore this method offers a significant time advantage over WDS-EPMA, particularly for extended analysis applications such as mapping or for very large sample sets. Advancements in SEM-EDX using field emission (FE-) and silicon drift detectors (SDD) have resulted in increased beam stability and a greater number of X-ray counts being detected with no compromise on spectral resolution.[21] Modern FE-SEM systems are able to produce an X-ray flux with a small, focused beam, typically <20 nm in diameter,[21] while modern SDD EDX detectors enable spatial resolution in the micro- to nano-range.[22] Low energy EDX mapping has been able to resolve sub-35 nm nanoparticles with a beam energy of 5 kV.[23] The spatial resolution of SEM-EDX, especially SDD-EDX, with its nanometer scale beam diameter is greater than that of WDS-EPMA, where the beam diameter is typically in the micron range (*e.g.*, ref. 14, 16 and 18). EPMA requires considerably higher beam current to achieve finer beam diameter, however it has long been known that an increased beam current results in elevated risk of mobilization of Na ions (*e.g.*, ref. 16, 24 and 25). The key spatial resolution advantage of SEM-EDX lends itself to analysis of discrete features such as tiny tephra shards, microlites and exsolution textures, all of which may be too small for WDS-EPMA.

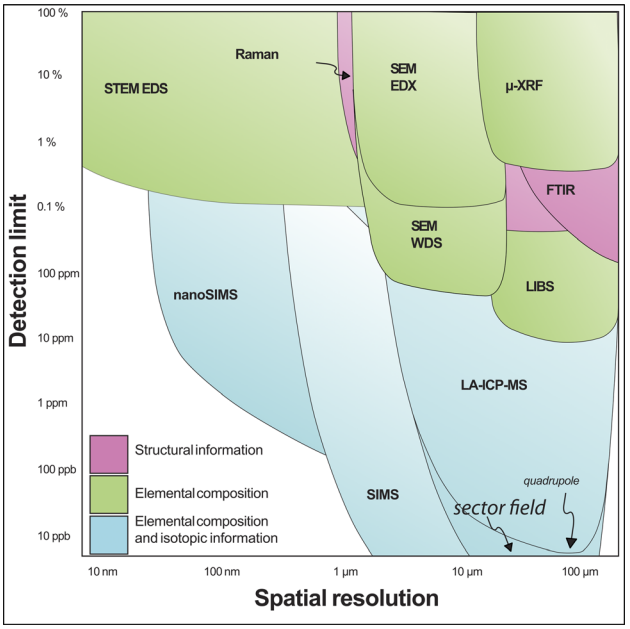

Fig. 1 Detection limit *vs.* spatial resolution (*x*-axis) for the suite of microbeam methods commonly utilised by geoscientists, adapted from Chew *et al.*[26] and Li and Li.[27]

SEM-EDX has similar detection limit to STEM EDS and µ-XRF, and similar spatial resolution to EPMA, Raman, SIMS and LA-ICP-MS (Fig. 1, adapted from ref. 26 and 27). This study provides a more thorough comparison of spatial resolution and detection limit between SEM-EDX and EPMA. SEM-EDX detectors can simultaneously acquire all elements present in the sample with the exception of H, He and Li.[28] However, there are difficulties attaining quantifiable data on the light elements Be, B, C, N, O and F due to X-ray peak overlaps, low fluorescence yield and contamination (*e.g.*, ref. 29). The issue of X-ray peak overlap is not just limited to the light elements; Newbury and Ritchie (2015)[1] highlight the overlap of S, Mo and Pb (S K at 2.307 keV, Mo L at 2.293 keV, and Pb M at 2.346 keV).

A significant hurdle that SEM-EDX must cross for acceptance in the wider analytical community is its reputation as merely a semi-quantitative technique. Arguably the primary cause for this mistrust was the rise of "standardless analysis", whereby the user relied on factory calibrations within the software used to interpret the EDX data. Using matrix-matched compound standards to create X-ray peak references to compare to the spectra of unknown samples can result in precision and accuracy comparable to that of WDS-EPMA.[21] Here, we evaluate the detection, spatial resolution, accuracy, and precision of SEM-EDX analysis for a range of glass rikeference materials and propose analytical protocols to optimise SEM-EDX data quality.

2. Samples

This study investigates a suite of well characterised magmatic glass reference materials that span a range of compositions from komatiite to rhyolite and with a range of alkali contents (SiO_2: 45.5–76.7; Na_2O: 0.83–4.44; K_2O: 0.19–5.10 wt%). These

glasses include the Smithsonian National Museum of Natural History (NMNH) glasses NMNH VG-2, NMNH 72854, NMNH 113498-1 and NMNH 113716-1,[30] MPI-DING glasses ATHO-G, T1-G, StHs6/80-G and GOR132-G,[31] as well as rhyolitic glasses ID3506 (ref. 32) and Oregon Obsidian from the MINM25-53 standard mount (ESI Table 1†). The glass samples employed in this study are of known composition and are widely used as reference materials in WDS-EPMA analyses of glasses (*e.g.*, ref. 33 and 34). The two glasses initially investigated to determine optimal experimental setup are the basaltic glass NMNH VG-2 and the rhyolitic glass NMNH 72854.[30] These were selected as two homogenous end members which span a broad compositional range. The MINM25-53 mount contains a suite of silicate and sulphide minerals, produced by Astimex Standards Ltd, Canada.

The study chose to focus on glass because it is non-stoichiometric, and thus presents a greater challenge than minerals for which stoichiometry provides an additional check on data quality (*e.g.*, ref. 35) and also because of the potential for beam-induced elemental mobility. Fully quantitative SEM-EDX analysis on glass thus requires careful instrument set-up while precise sample preparation is needed to account for issues with specimen geometry. Samples were polished on an automatic lap using progressively finer diamond grits down to 1 micron to ensure a flat and highly polished surface to attain fully quantitative SEM-EDX results. The samples also need to be fully conductive to avoid charging of electrons on the surface, typically this will require specimens to be coated in a thin layer of carbon or gold. All samples were coated with 12 nm of carbon before being introduced into the SEM chamber for analysis. Finally, additional analyses were undertaken on natural volcanic glass shards to further highlight SEM-EDX data quality and to demonstrate some of the advantages offered by this technique. These samples include:

- Tephra layer TM-24-3b from an eruption of Ischia and deposited at Lago Grande di Monticchio, Italy (LGdM) (ref. 36 and 37) 80 km to the east. This sample was previously analysed by EPMA[37] and is reanalysed here by SEM-EDX to allow comparison of the data quality achieved by the two techniques.
- Mafic tephra from the PdB (Pomici di Base) eruption of Somma-Vesuvius which is challenging to analyse because the tephra is microlite rich[38] and the spacing between microlites is smaller than the interaction volume produced by a 10 μm beam. This resulted in the acquisition of mixed compositions (glass and crystal phases) with the EPMA method (ref. 39: their Fig. 7).
- Basaltic cryptotephra shards from the Laki 1783-84 AD eruption identified in Brackloon Wood, Co. Mayo, Ireland (ref. 40 and 41). Analysis of these tephra presents a challenge because of their extremely small size (<40 μm vesicular shards with analyzable areas of <20 μm) and only two out of 24 were successfully analysed by EPMA.[42]

3. Methodology

This study uses a Tescan S-8000 FE-SEM operating under high vacuum conditions, fitted with four 170 mm^2 Ultim Max EDX detectors running the Oxford Instruments AZtec microanalysis software version 5.1 (and subsequently version 6.1) at the iCRAG Laboratory in Trinity College Dublin. Additional analyses were undertaken using a Tescan Tiger Mira3 FE-SEM operating under high vacuum conditions, fitted with two XMax^n 150 mm^2 EDX detectors running Oxford Instruments AZtec microanalysis software version 3.2. Unless otherwise specified, analyses were undertaken with a voltage of 20 kV, a 4.5 nm wide beam with beam current of 300 pA, and a process time of five, following the SEM-EDX protocol defined in Ubide *et al.* (2017).[8] Beam current drift was controlled by analysis of cobalt after each sample change, however it is worth noting that modern FE-SEMs show considerably lower drift compared to older W-SEM systems.[43] Process time is a dimensionless time index between one and six within the AZtec software. It is a time index where a lower number prioritises analysis time and a higher number prioritizes energy resolution.

Fully quantified SEM-EDX analysis requires the microscope to be set up correctly and to have the highly-polished and flat sample under the beam at an appropriate working distance (WD) which herein is 15 mm. There are two main ways to collect SEM-EDX spectra through AZtec; Analysis Mode or Point & ID. Analysis mode collects data by rastering a 4.5 nm beam over the scanning window for a determined runtime and collecting all X-ray information within this field of view at a high magnification while Point & ID collects a reference image such as back-scattered electron (BSE) at a lower magnification and analysis is acquired from selected areas within this image. The selected area can be a selected point or a shape (*e.g.*, a circle, rectangle, or user-defined polygon). The acquisition of an image showing the location of the SEM-EDX spot analyses when using the Point & ID method makes it initially quite appealing; however, there are drawbacks with this approach. In practice, due to the resolution of the acquired image at lower magnification, it is not always possible to ensure that the sample is polished completely flat. In mineral samples, there may be material removed along grain boundaries or along cleavage planes and such areas need to be avoided. Accurate and fully quantitative SEM-EDX analysis requires flat, polished samples that are in-focus which is not always possible during Point & ID spot analysis; a very well-polished geologic sample may still have varying topography. Analysis Mode ensures that the sample is in-focus, thus providing more confidence in the quality of the analysis. In both methods it is possible to collect the data using a set runtime or until a set number of counts has been attained.

X-ray peak energies for each peak were calibrated to concentrations using a range of mineral and glass standards. For optimal matrix matching of silicate glasses, we used the following phases on the Astimex MINM25-53 standard mount for standardisation: apatite, chromite, diopside, kaersutite, magnetite, olivine, orthoclase, pentlandite, rhodonite, rutile and tugtupite (ESI Table 1†). All chemical data presented in this study are presented as oxide weight percent where oxygen has been calculated by stoichiometry in AZtec, with the exception of Cl (element %). Standard phases were analysed for 2M counts, and as the instrument is collecting 100k counts per second, and has a dead time of c. 15%, each analysis took approximately 25

seconds. Standardisation is undertaken at the start of each day/session.

Following SEM setup for fully quantified EDX analysis, experiments were first undertaken to optimise the number of counts and the width of the field of view, using basaltic glass NMNH VG-2 and the rhyolitic glass NMNH 72854. The number of counts collected were 10k, 20k, 50k, 100k, 200k, 500k, 1M, 2M, 5M and 10M. Lower counts equate to faster analyses but with lower precision compared to higher counts, while higher counts result in potential loss of mobile, volatile elements (Na, K, Cl). To quantify the risk of loss of mobile and volatile elements, consecutive analysis under increasing count times on both the basaltic and rhyolitic glasses was undertaken. Analyses totalling 1M, 2M, 5M and 10M counts were acquired by repeated spot analysis (20, 10, 4 and 2 times respectively) over the same spot until a total of 20M counts were collected. Next, an experiment into spatial resolution of SEM-EDX at the specified instrument conditions was undertaken. The field of view (FoV) was changed from 0.1 μm to 50 μm (expressed in terms of its width with the FoV typically having a 1 : 1 or 4 : 3 aspect ratio), to determine the smallest feature that can be analysed with fully quantitative EDX without resulting in potential loss of mobile and/or volatile elements. Following optimisation, accuracy and precision was assessed through 25 spot analyses on all studied glasses. Finally, additional analyses were undertaken on the following natural volcanic glass shards:

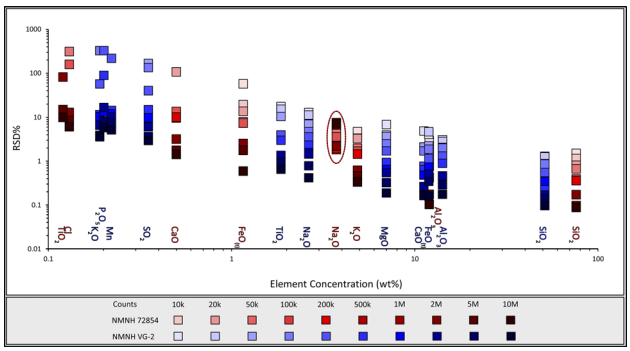

Fig. 2 Spot analyses on basaltic glass NMNH VG-2 and rhyolitic glass NMNH 72854 collected over a range of counts to determine the optimal number of counts required for best precision. Element concentration (oxide wt%) *vs.* RSD%. Na_2O in NMNH 72854 is highlighted.

Thirty-nine tephra shards were analysed across the tephra band TM-24-3b in the polished thin section J45.3.1B. 30 of the 39 tephra shards (TM24-3b_P1 to TM24-3b_P30) were analysed on Tescan S-8000 FE-SEM and the remaining nine (TM24-3b_V1 to TM24-3b_V9) were analysed on a Tescan Tiger Mira3 FE-SEM. Both SEMs were set up identically with the same working distance, voltage, beam current, counts per analysis and scanning FoV.

Forty analyses of the microlite-rich glass PM21 from the Pomici di Base eruption were collected on the Tescan S-8000 FE-SEM, using the same working distance, voltage, beam current

Table 1 Average oxide wt% of spot analysis on the basaltic glass NMNH VG-2 and the NMNH rhyolitic glass NMNH 72854 acquired for a specified number of counts ranging from 10k to 10M

Counts	10k	20k	50k	100k	200k	500k	1M	2M	5M	10M
NMNH VG-2										
SiO_2	49.8	50.6	50.6	50.8	50.7	50.6	50.7	50.7	51.1	50.7
Al_2O_3	13.8	13.9	13.8	13.8	13.8	13.9	13.9	13.8	14.0	13.8
FeO(t)	11.4	11.7	11.7	11.7	11.7	11.7	11.8	11.7	11.9	11.7
CaO	10.7	10.9	10.9	10.9	10.9	10.9	10.9	11.0	11.0	11.0
MgO	6.64	6.64	6.88	6.84	6.80	6.83	6.81	6.83	6.88	6.80
Na_2O	2.80	2.69	2.65	2.72	2.73	2.74	2.71	2.70	2.69	2.69
TiO_2	1.75	1.78	1.90	1.90	1.91	1.87	1.88	1.88	1.89	1.88
SO_2	0.00	0.00	0.19	0.20	0.36	0.37	0.37	0.37	0.36	0.38
MnO	0.00	0.00	0.00	0.00	0.05	0.22	0.21	0.22	0.23	0.21
P_2O_5	0.00	0.00	0.00	0.06	0.04	0.16	0.21	0.21	0.18	0.22
K_2O	0.00	0.04	0.03	0.02	0.16	0.19	0.19	0.19	0.22	0.19
Cr_2O_3	<LOD	<LOD	<LOD	<LOD	<LOD	<LOD	<LOD	0.02	0.00	0.07
Cl	<LOD	<LOD	<LOD	<LOD	<LOD	<LOD	<LOD	<LOD	0.02	0.03
Total	97.00	98.16	98.48	98.74	98.82	99.15	99.25	99.18	100.04	99.24
NMNH 72854										
SiO_2	76.3	76.9	77.1	77.3	77.3	77.4	77.4	77.9	77.9	78.1
Al_2O_3	11.9	12	12.1	12.2	12.2	12.2	12.1	12.2	12.2	12.2
K_2O	4.95	4.84	4.94	5.01	4.93	4.94	4.95	5.07	5.08	5.08
Na_2O	3.67	3.5	3.44	3.37	3.17	3.7	3.53	2.99	2.91	3.28
FeO(t)	1.02	1.11	1.22	1.12	1.15	1.2	1.17	1.18	1.18	1.18
CaO	0.00	0.00	0.26	0.44	0.47	0.47	0.45	0.48	0.48	0.47
Cl	<LOD	<LOD	<LOD	0.02	0.04	0.11	0.12	0.12	0.11	0.11
TiO_2	<LOD	<LOD	<LOD	<LOD	<LOD	<LOD	0.01	0.05	0.08	0.09
MgO	<LOD	<LOD	<LOD	<LOD	<LOD	<LOD	<LOD	0.01	0.01	0.01
MnO	<LOD	<LOD	<LOD	<LOD	<LOD	<LOD	<LOD	<LOD	<LOD	0.01
P_2O_5	<LOD	<LOD	<LOD	<LOD	<LOD	<LOD	<LOD	<LOD	<LOD	<LOD
Total	97.84	98.35	99.06	99.46	99.26	100.02	99.73	100.00	99.95	100.53

and counts per analysis. However, these analyses were completed with a scanning FoV of 1 μm to avoid partial analysis of microlites. An EDX map and BSE image were collected to highlight the microlite density. The voltage and working distance remained as before but the beam current was increased to 3 nA to offset the effect of the smaller FoV on the total number of counts and the process time was set to 2. This increased beam current increases the SEM counts per second to approximately 800 kcps. For the map, the field of view was set to 50 μm. Both a BSE image and an EDX map were collected with a resolution of 2048 × 1557, with a pixel dwell time of 10 μs per pixel for the BSE image and 200 μs per pixel for the EDX map.

The cryptotephra from the Laki 1783-84 AD eruption was analysed using a wavelength-dispersive JEOL 8600 electron microprobe in 2016. This analysis was completed using an accelerating voltage of 15 kV, a 6 nA current and a beam diameter of 10 μm. Peak count times were 30 s for most elements and 10 s for Na. Due to the small size (25–40 μm long but with analyzable areas of <20 μm) of the cryptotephra, only one EPMA analysis was acquired successfully.[42] The cryptotephra samples were reanalysed in the same year by SEM-EDX using a Tescan Mira XMU FE-SEM equipped with an Oxford Instruments X-Max 80 mm^2 EDX detector and Oxford Inca software. In total, nine basaltic shards were analysed.[42]

4. Results and discussion

4.1 Optimal number of counts

The number of counts per analysis is a trade-off between sensitivity on the one hand and acquisition runtime and cation mobilisation on the other. Fig. 2 shows the relative standard deviations (RSD%) of SEM-EDX glass analyses conducted over a range of total counts (complete data can be found in Table 1 and ESI Table 1†). For almost all elements the most precise results came from the analyses that collected the highest number of counts. The quickest analyses, those acquired with 10k and 20k counts (below one second analysis time), displayed relative standard deviation (RSD%) >5% on elements over 10 wt oxide%, and RSD% >10% on elements above 1 wt oxide%. Once the number of counts per analysis is above 100k (one to three second analysis time), all elements over 1.5 wt oxide% exhibited a RSD% of <5%. These results here may have implications on fully quantifiable alternative SEM-EDX applications such as element mapping, where analysis of large cumulative areas necessitates rapid analysis. When >1M counts were acquired, the RSD% for major element oxides was <2% for both basaltic glass VG-2 and rhyolitic glass NMNH 72854. For fully quantitative EDX analysis, we recommend collecting a minimum of 1M counts, as this will result in rapid acquisition (approximately 15 seconds using the above SEM parameters) of accurate major element data. It is possible to attain data of similar precision for higher concentration trace elements (those present at >0.1 wt% or above) in both glasses, but this requires analyses of c. 10M counts.

Certain elements (*e.g.*, Na, K and Cl), are known to display mobility during beam interaction due to heating.[15,16,25] However, it is evident from Fig. 2 that the precision of Na analyses in rhyolite glass NMNH 72854 was adversely affected only at high counts (≥5M). Even lower beam currents can result in Na-loss over an extended period of time.[16] Hence, to

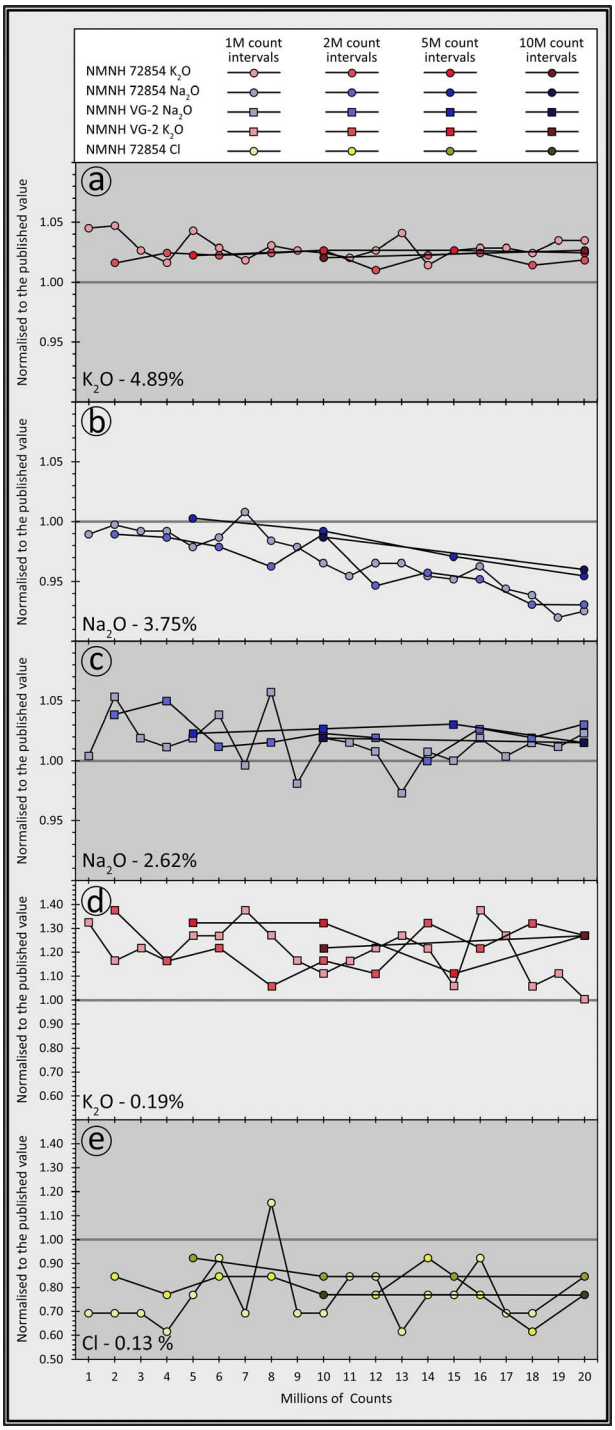

Fig. 3 Repeat analyses on basaltic NMNH VG-2 and rhyolitic glass NMNH 72854 to investigate potential beam-induced elemental loss on Na_2O, K_2O and Cl. Each glass is analysed in four separate areas up to a total of 20M counts. Analyses comprised either 1M, 2M, 5M and 10M count intervals. Panels (a)–(e) display analyses on elements in decreasing abundance. K_2O in NMNH 72854 and Na_2O in both glasses are major elements (panels (a)–(c)), and the remaining K_2O (NMNH VG-2) and Cl (NMNH 72854) analyses are minor elements (panels (d) and (e)).

Table 2 Repeated spot analysis on NMNH VG-2 and NMNH 72854. For each glass four separate areas were analysed summing up to a total of 20M counts

Counts (million)	1	1	1	1	1	1	1	1	1	1	1	1
NMNH VG-2	**33a**	**33b**	**33c**	**33d**	**33e**	**33f**	**33g**	**33h**	**33i**	**33j**	**33k**	**33l**
SiO_2	50.7	50.8	51.0	51.1	50.8	51.0	51.0	51.0	51.0	51.1	51.1	51.1
Al_2O_3	14.1	14.2	14.2	14.1	14.1	14.1	14.2	14.1	14.1	14.2	14.1	14.2
FeO(t)	11.7	11.7	11.6	11.7	11.8	11.6	11.6	11.4	11.7	11.8	11.6	11.6
CaO	11.1	11.1	11.1	11.2	11.1	11.1	11.1	11.2	11.1	11.2	11.2	11.2
MgO	7.00	6.93	6.93	7.06	7.02	6.89	6.96	6.86	7.00	6.94	6.94	6.91
Na_2O	2.63	2.76	2.67	2.65	2.67	2.72	2.61	2.77	2.57	2.67	2.66	2.64
TiO_2	1.93	1.90	1.88	1.87	1.90	1.89	1.98	1.89	1.88	1.95	1.88	1.92
SO_2	0.37	0.43	0.37	0.32	0.35	0.35	0.38	0.33	0.40	0.34	0.35	0.37
MnO	0.20	0.16	0.26	0.30	0.20	0.24	0.23	0.25	0.21	0.22	0.27	0.25
P_2O_5	0.25	0.00	0.24	0.27	0.22	0.00	0.29	0.23	0.25	0.00	0.30	0.00
K_2O	0.25	0.22	0.23	0.22	0.24	0.24	0.26	0.24	0.22	0.21	0.22	0.23
Cr_2O_3	0.00	0.00	0.00	0.00	0.00	0.00	0.00	0.00	0.00	0.00	0.00	0.00
Cl	0.00	0.00	0.00	0.00	0.00	0.00	0.00	0.00	0.00	0.00	0.00	0.00
Total	100.17	100.28	100.50	100.85	100.43	100.17	100.57	100.22	100.50	100.51	100.67	100.40
NMNH 72854	**37a**	**37b**	**37c**	**37d**	**37e**	**37f**	**37g**	**37h**	**37i**	**37j**	**37k**	**37l**
SiO_2	77.6	77.6	77.5	77.4	77.4	77.6	77.7	77.3	77.2	77.7	77.5	77.4
Al_2O_3	12.3	12.4	12.4	12.4	12.3	12.4	12.5	12.3	12.3	12.4	12.3	12.5
K_2O	5.11	5.12	5.02	4.97	5.10	5.03	4.98	5.04	5.02	5.01	4.99	5.02
Na_2O	3.71	3.74	3.72	3.72	3.67	3.70	3.78	3.69	3.67	3.62	3.58	3.62
FeO(t)	1.10	1.02	1.12	1.02	1.08	1.04	1.10	1.07	1.03	1.07	1.09	1.07
CaO	0.45	0.43	0.48	0.44	0.48	0.42	0.43	0.42	0.38	0.48	0.43	0.46
Cl	0.09	0.09	0.09	0.08	0.10	0.12	0.09	0.15	0.09	0.09	0.11	0.11
TiO_2	0.00	0.00	0.00	0.00	0.00	0.00	0.00	0.00	0.00	0.00	0.13	0.00
MgO	0.00	0.00	0.00	0.00	0.00	0.00	0.00	0.00	0.00	0.00	0.00	0.00
MnO	0.00	0.00	0.00	0.00	0.00	0.00	0.00	0.00	0.00	0.00	0.00	0.00
P_2O_5	0.00	0.00	0.00	0.00	0.00	0.00	0.00	0.00	0.00	0.00	0.00	0.00
Total	100.35	100.39	100.28	99.99	100.18	100.28	100.61	99.99	99.73	100.43	100.15	100.24

Counts (million)	1	1	1	1	1	1	1	1	2	2	2	2
NMNH VG-2	**33m**	**33n**	**33o**	**33p**	**33q**	**33r**	**33 s**	**33 t**	**34a**	**34b**	**34c**	**34d**
SiO_2	50.9	50.9	51.2	50.8	51.1	50.9	50.8	50.8	51.3	51.1	51.2	51.3
Al_2O_3	14.1	14.1	14.1	14.0	14.2	14.3	14.1	14.3	14.3	14.2	14.2	14.2
FeO(t)	11.6	11.6	11.8	11.7	11.7	11.7	11.8	11.8	11.8	11.8	11.8	11.8
CaO	11.2	11.3	11.2	11.2	11.2	11.2	11.2	11.2	11.3	11.2	11.3	11.3
MgO	6.99	6.93	7.00	6.98	7.00	7.08	6.81	6.94	7.07	7.06	7.01	6.99
Na_2O	2.55	2.64	2.62	2.67	2.63	2.66	2.65	2.68	2.72	2.75	2.65	2.66
TiO_2	1.95	1.93	1.85	1.84	1.88	1.86	1.95	1.93	1.90	1.92	1.91	1.90
SO_2	0.42	0.43	0.36	0.44	0.42	0.46	0.31	0.37	0.33	0.37	0.42	0.40
MnO	0.23	0.18	0.18	0.20	0.23	0.25	0.29	0.21	0.25	0.24	0.21	0.23
P_2O_5	0.22	0.27	0.00	0.00	0.00	0.00	0.23	0.00	0.24	0.26	0.23	0.21
K_2O	0.24	0.23	0.20	0.26	0.24	0.20	0.21	0.19	0.26	0.22	0.23	0.20
Cr_2O_3	0.00	0.00	0.00	0.00	0.00	0.00	0.00	0.00	0.00	0.00	0.00	0.00
Cl	0.00	0.00	0.00	0.00	0.00	0.00	0.00	0.00	0.00	0.00	0.00	0.00
Total	100.35	100.47	100.50	99.99	100.41	100.60	100.34	100.37	101.44	101.09	101.08	101.23
NMNH 72854	**37m**	**37n**	**37o**	**37p**	**37q**	**37r**	**37 s**	**37 t**	**38a**	**38b**	**38c**	**38d**
SiO_2	77.6	77.7	77.5	77.5	77.5	77.5	77.7	77.7	77.5	77.1	77.4	77.2
Al_2O_3	12.4	12.5	12.4	12.4	12.4	12.5	12.4	12.4	12.3	12.4	12.3	12.4
K_2O	5.09	4.96	5.02	5.03	5.03	5.01	5.06	5.06	4.97	5.01	5.00	5.01
Na_2O	3.62	3.58	3.57	3.61	3.54	3.52	3.45	3.47	3.71	3.70	3.67	3.61
FeO(t)	1.04	1.08	1.07	1.01	1.11	1.06	1.04	1.12	1.08	1.14	1.09	1.08
CaO	0.38	0.48	0.43	0.40	0.41	0.44	0.43	0.46	0.44	0.43	0.47	0.44
Cl	0.08	0.10	0.10	0.12	0.09	0.09	0.00	0.11	0.11	0.10	0.11	0.11
TiO_2	0.00	0.00	0.00	0.00	0.00	0.00	0.00	0.13	0.13	0.09	0.00	0.12
MgO	0.00	0.00	0.00	0.00	0.00	0.00	0.00	0.00	0.00	0.00	0.00	0.00
MnO	0.00	0.00	0.00	0.00	0.00	0.00	0.00	0.00	0.00	0.00	0.00	0.00
P_2O_5	0.00	0.00	0.00	0.00	0.00	0.00	0.00	0.00	0.00	0.00	0.00	0.00

Table 2 (*Contd.*)

Counts (million)	2	2	2	2	2	2	5	5	5	5	10	10
NMNH VG-2	**34e**	**34f**	**34g**	**34h**	**34i**	**34j**	**35a**	**35b**	**35c**	**35d**	**36a**	**36b**
SiO_2	51.3	51.4	51.3	51.3	51.4	51.2	51.3	51.3	51.3	51.4	51.3	51.2
Al_2O_3	14.3	14.3	14.2	14.3	14.3	14.2	14.2	14.3	14.2	14.2	14.2	14.2
FeO(t)	11.8	11.8	11.8	11.8	11.8	11.8	11.8	11.8	11.8	11.8	11.9	11.8
CaO	11.2	11.2	11.3	11.3	11.3	11.3	11.3	11.2	11.3	11.2	11.2	11.2
MgO	7.10	6.92	7.08	7.00	7.05	6.97	6.98	6.97	7.00	6.98	6.97	6.95
Na_2O	2.68	2.67	2.62	2.69	2.67	2.70	2.68	2.69	2.70	2.66	2.67	2.66
TiO_2	1.94	1.91	1.91	1.89	1.95	1.96	1.91	1.93	1.90	1.90	1.89	1.91
SO_2	0.35	0.38	0.32	0.38	0.40	0.43	0.37	0.41	0.40	0.34	0.36	0.41
MnO	0.20	0.23	0.24	0.23	0.26	0.27	0.23	0.22	0.23	0.22	0.23	0.23
P_2O_5	0.24	0.17	0.18	0.24	0.23	0.19	0.27	0.24	0.18	0.24	0.22	0.18
K_2O	0.22	0.21	0.25	0.23	0.25	0.24	0.25	0.25	0.21	0.24	0.23	0.24
Cr_2O_3	0.00	0.00	0.00	0.00	0.00	0.00	0.00	0.00	0.00	0.00	0.00	0.00
Cl	0.00	0.00	0.05	0.00	0.00	0.00	0.03	0.04	0.00	0.00	0.03	0.03
Total	101.33	101.24	101.09	101.33	101.57	101.31	101.26	101.36	101.28	101.18	101.21	101.00
NMNH 72854	**38e**	**38f**	**38g**	**38h**	**38i**	**38j**	**39a**	**39b**	**39c**	**39d**	**40a**	**40b**
SiO_2	77.1	77.2	77.2	77.1	77.2	77.2	77.3	77.2	77.3	77.4	77.2	77.3
Al_2O_3	12.3	12.3	12.3	12.4	12.3	12.3	12.3	12.4	12.4	12.4	12.4	12.4
K_2O	5.02	4.94	5.00	5.01	4.96	4.98	5.00	5.02	5.02	5.01	4.99	5.02
Na_2O	3.71	3.55	3.59	3.57	3.49	3.49	3.76	3.72	3.64	3.58	3.70	3.60
FeO(t)	1.12	1.11	1.12	1.11	1.16	1.08	1.15	1.16	1.15	1.14	1.14	1.15
CaO	0.43	0.43	0.44	0.44	0.46	0.46	0.44	0.44	0.46	0.45	0.45	0.45
Cl	0.10	0.10	0.12	0.10	0.08	0.10	0.12	0.11	0.11	0.11	0.10	0.10
TiO_2	0.00	0.10	0.00	0.00	0.00	0.00	0.06	0.08	0.09	0.07	0.07	0.07
MgO	0.00	0.00	0.00	0.00	0.00	0.00	0.00	0.00	0.00	0.00	0.00	0.00
MnO	0.00	0.00	0.00	0.00	0.00	0.00	0.00	0.00	0.00	0.00	0.04	0.05
P_2O_5	0.00	0.00	0.00	0.00	0.00	0.00	0.00	0.00	0.00	0.00	0.00	0.00
Total	99.79	99.71	99.72	99.65	99.64	99.64	100.13	100.13	100.13	100.14	100.08	100.07

investigate mobile element loss because of beam damage, repeated spot analysis on the same position, summing up to 20M counts in total, was undertaken on NMNH glasses 72 854 and VG-2 (Fig. 3 and Table 2). K_2O is a major element in rhyolite NMNH 72854 (Fig. 3a) and a minor element in basalt NMNH VG-2 (Fig. 3d), and there does not appear to be any loss in K concentration with increasing counts across the investigated count range. Chlorine is a minor element in the rhyolitic glass at 0.13 wt%, and a trace element in the basaltic glass at 0.03 wt%.

There is no noticeable Cl depletion in the rhyolitic glass over time, yet it is significantly below the published value of 0.13 wt% (Fig. 3e). Cl in the basaltic glass is below detection at 1M and 2M counts but is detected at 5M and 10M counts. Na_2O is a major element in both the NMNH VG-2 basalt (Fig. 3c) and 72 854 rhyolite (Fig. 3b) glasses at 2.62 wt% and 3.75 wt%, respectively. There is no noticeable Na loss in the basaltic glass, even at 10M counts. The measured Na_2O content of NMNH 72854 rhyolite begins to decrease after approximately 5M counts and continues to decrease with further analysis such that by 20M counts the analysed concentration is approximately 5% lower than it was at 5M counts. The Na loss affecting the rhyolitic glass over the basaltic glass is due to the higher concentration of H_2O and the lower abundance of other network modifying cations (*e.g.*, Fe^{2+}, Mg, Mn, *etc.*).[25] With the SEM setup at 20 kV and 300 pA, it takes approximately one minute to acquire 5M counts when using four 170 mm^2 Ultim Max EDX detectors. Sodium mobility puts an upper limit on the optimal number of counts for analysis of glass, but under standard analytical conditions the mobility of these elements is not a concern. We recommend that with a beam current of 300 pA, high precision fully quantitative SEM-EDX analysis should be at least 1M counts and at most 5M.

4.2 Analysis area

SEM-EDX and EPMA analysis at 20 kV results in penetration range of electrons in silicate minerals to a depth of less than 4.5 μm,[44] to ensure homogenous analysis the area being analysed must be greater than the range. The surface radius must be equal or lower than the range. Monte Carlo simulations for a 20 kV accelerating voltage show an interaction volume with a diameter of approximately the same diameter on the surface. The following formula, modified from ref. 44, can be used to calculate the range (R):

$$R(\mu\text{m}) = \frac{0.0276 \times A \times E^{1.67}}{\rho \times Z^{0.89}}$$

where A is the atomic mass (g mol^{-1}), E is the accelerating voltage (keV), ρ is the density (g cm^{-3}) and Z is the atomic number.

Range decreases as atomic number and density increases, so denser basaltic glass would have lower interaction volume than

the less dense rhyolitic glass. As silicate minerals are compounds rather than individual elements, it is necessary to calculate effective atomic number and effective atomic mass. One can calculate effective atomic number Z_{eff} using Mayneord's definition:[45]

$$Z_{\text{eff}} = \sqrt[2.94]{\sum f_{\text{n}} \times (Z_{\text{n}})^{2.94}}$$

where f_{n} is the fraction of the total number of electrons associated with each element and Z_{n} is the atomic number of each element. The effective atomic mass (A_{eff}) can be calculated using the following formula:

$$A_{\text{eff}} = \Sigma(f_{\text{n}} \times A_{\text{n}})$$

where f_{n} is the fraction of the total number of electrons associated with each element and A_{n} is the atomic mass of each element.

Silicate minerals display a range of less than 4 μm; quartz, albite, anorthite and fayalite have ranges of approximately 3.80 μm, 3.9 μm, 3.61 μm and 1.63 μm respectively at 20 kV. The spatial resolution of analysis, or analytical resolution (D_{AR}), is defined by the following formula:

$$D_{\text{AR}} = ({D_{\text{beam}}}^2 + {D_{\text{emission}}}^2)^{1/2}$$

where D_{beam} is the diameter of the beam and D_{emission} is the surface diameter of the X-ray generated volume.[46] SEM-EDX analysis at c. 300 pA generates a fine beam diameter (<20 nm; ref. 21). At such a small beam diameter, the interaction volume controls the spatial resolution of analysis, which is then better than 4 μm for silicate matrices. By contrast, an EPMA beam diameter is typically in the low micron range for high sensitivity applications (*e.g.*, ref. 14), or > 10 μm for standard analysis (*e.g.*, ref. 16 and 18). The spatial resolution of the high sensitivity EPMA outlined by Batanova *et al.* (2018),[14] employing a FoV of 1 μm, is comparable to SEM-EDX under the conditions described above, however the high beam current employed can lead to damage of beam-sensitive material such as glass. The spatial resolution of standard EPMA analysis where the beam has been widened to >10 μm (*e.g.* ref. 16 and 18) is up to 10% wider than the diameter of the beam on silicate minerals. This provides SEM-EDX a significant spatial resolution advantage over EPMA.

Analysis mode collects data by rastering over a set scanning area. To determine the optimal scanning area for raster analysis, the basaltic and rhyolitic glasses were again analysed at the following FoVs; 0.1 μm, 1 μm, 5 μm, 10 μm and 50 μm (FoV width quoted with an aspect ratio of 4 : 3). The interaction volume diameters for each of these FoVs are approximately 4.1 μm, 5 μm, 9 μm, 14 μm and 54 μm respectively. For each FoV, ten analyses were acquired at 1M counts. Fig. 4a highlights the precision of analyses on both the basaltic and rhyolitic glasses using these varying scanning areas (data found in ESI Table 1†). Major element (*i.e.*, >1 wt%) precision is excellent (<2.5 RSD%) in all glass FoV analyses with only one exception – FeO(t) in the rhyolitic glass NMNH 72854. This may be due to reported impurities of c. 5 μm crystals of iron oxide.[30] Accuracy (Fig. 4b) of all major elements in the basaltic glass NMNH VG-2 is

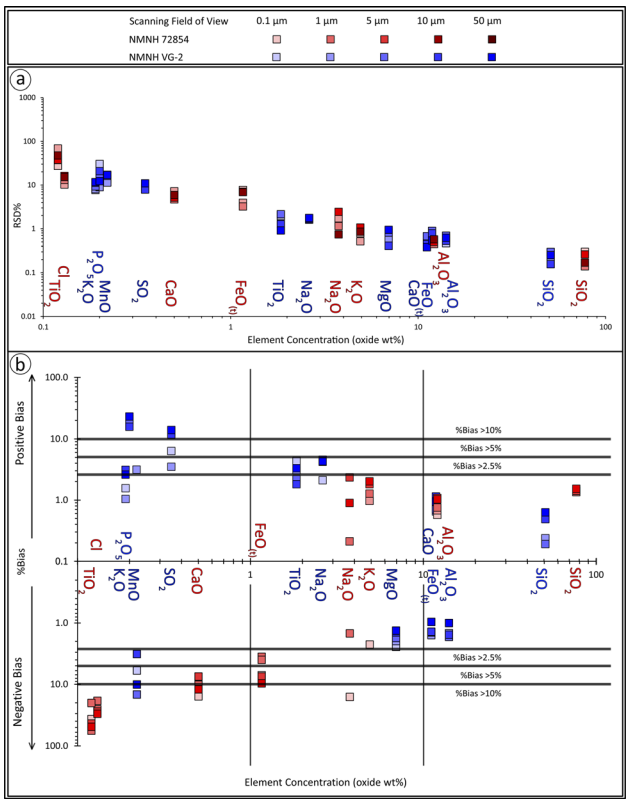

Fig. 4 Spot analyses on basaltic glass NMNH VG-2 and rhyolitic glass NMNH 72854 collected for a range of field of views to determine the optimal scanning FoV required for best precision (a) and accuracy (b). The full dataset is found in ESI Table 1.†

excellent with %bias <2.5% for all elements >10 oxide wt% and <5% for all remaining major elements. Sodium displays volatile loss with a FoV of 0.1 μm due to focusing of energy onto a small area, an effect seen in hydrous glasses.[25] The issues with Na loss are resolved with a FoV of 1 μm or larger as the beam energy is distributed over a wider area, and major elements in the 1–3 oxide wt% range display marginal improvement in precision with a wider FoV.

With a FoV set to 5 μm and following the SEM-EDX interaction volume calculations outlined above, features as small as 9 μm in diameter can be analysed quantitatively, assuming the

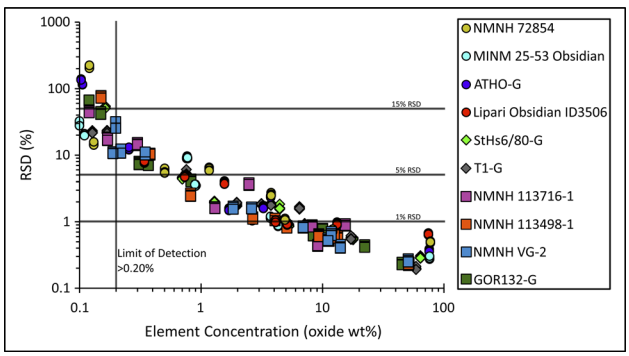

Fig. 5 Spot analysis on a suite of natural glasses (ESI Table 1†) displaying the precision using a scanning FoV of 5 μm and for 1M counts.

Table 3 Precision (RSD%) and accuracy (%Bias) of spot analyses on a range of well characterised glasses (ESI Table 1) at 5 μm FoV and collected for 1M counts. Full data for the spot analyses is presented in ESI Table 1

NMNH 72854	Jarosewich *et al.*, 1980[30]	Mean	2SD	RSD%	2SD	%Bias	MINM25-53 obsidian	MINM-35-53	Mean	2SD	RSD%	2SD	%Bias
SiO_2	76.7	77.2	0.76	0.49	0.02	0.61	SiO_2	76.3	75.4	0.43	0.28	0.02	−1.12
Al_2O_3	12.1	12.1	0.17	0.72	0.03	0.34	Al_2O_3	13.0	12.9	0.17	0.65	0.02	−1.12
K_2O	4.89	5.01	0.11	1.09	0.04	2.37	K_2O	4.31	4.40	0.08	0.88	0.05	2.17
Na_2O	3.75	3.61	0.18	2.52	0.13	−3.60	Na_2O	3.74	3.82	0.09	1.16	0.05	2.01
$FeO_{(t)}$	1.16	1.14	0.13	5.93	0.37	−2.06	CaO	0.88	0.88	0.06	3.55	0.14	−0.32
CaO	0.50	0.45	0.05	5.49	0.44	−9.34	$FeO_{(t)}$	0.76	0.82	0.15	9.09	0.40	7.37
Cl	0.13	0.11	0.03	14.4	0.80	−15.1	TiO_2	0.11	0.15	0.06	20.1	0.87	33.8
TiO_2	0.12	0.02	0.08	207	12.6	−83.0	MgO	0.10	0.11	0.06	28.4	2.36	5.60
MgO	0.09	0.00	0.00			−100	MnO	0.05	0.05	0.06	62.9	3.23	−2.40
MnO	0.03	0.00	0.00			−100	Total	99.27	98.53				
P_2O_5	0.01	0.00	0.00			−100							
Total	99.45	99.62											

ATHO-G	Jochum *et al.*,[31] 2011	Mean	2SD	RSD%	2SD	%Bias	Lipari obsidian ID3506	Kuehn *et al.*, 2011	Mean	2SD	RSD%	2SD	%Bias
SiO_2	75.6	74.0	0.53	0.36	0.02	−2.05	SiO_2	74.1	73.1	0.94	0.64	0.03	−1.41
Al_2O_3	12.2	11.9	0.15	0.63	0.03	−2.25	Al_2O_3	13.1	12.9	0.23	0.89	0.05	−1.51
Na_2O	3.75	4.10	0.19	2.38	0.10	9.26	K_2O	5.10	5.28	0.10	0.91	0.04	3.61
$FeO_{(t)}$	3.27	3.27	0.11	1.62	0.09	−0.06	Na_2O	4.07	4.01	0.08	0.99	0.05	−1.44
K_2O	2.64	2.68	0.06	1.06	0.06	1.44	$FeO_{(t)}$	1.55	1.56	0.12	3.75	0.23	0.52
CaO	1.70	1.73	0.05	1.51	0.08	1.51	CaO	0.73	0.76	0.07	4.72	0.21	3.78
TiO_2	0.26	0.26	0.06	12.3	0.63	1.80	Cl	0.34	0.33	0.05	7.70	0.51	−1.53
MnO	0.11	0.05	0.13	115	1.36	−48.3	TiO_2	0.07	0.07	0.05	33.8	1.84	1.08
MgO	0.10	0.04	0.12	137	3.41	−59.2	MnO	0.07	0.06	0.05	38.6	1.82	−7.08
P_2O_5	0.03						MgO	0.04	0.04	0.04	50.3	2.23	−7.32
Total	99.65	98.10					Total	99.17	98.08				

StHs6/80-G	Jochum *et al.*,[31] 2011	Mean	2SD	RSD%	2SD	%Bias	TG-1	Jochum *et al.*,[31] 2011	Mean	2SD	RSD%	2SD	%Bias
SiO_2	63.7	62.7	0.36	0.29	0.01	−1.55	SiO_2	58.6	58.4	0.23	0.19	0.01	−0.31
Al_2O_3	17.8	18.0	0.20	0.55	0.02	0.88	Al_2O_3	17.1	17.5	0.19	0.55	0.03	2.53
CaO	5.28	5.28	0.09	0.87	0.03	−0.05	CaO	7.10	7.06	0.12	0.87	0.05	−0.55
Na_2O	4.44	4.47	0.14	1.58	0.12	0.63	$FeO_{(t)}$	6.44	6.40	0.20	1.58	0.07	−0.65
$FeO_{(t)}$	4.37	4.36	0.09	1.01	0.05	−0.34	MgO	3.75	3.68	0.13	1.80	0.09	−1.83
MgO	1.97	1.91	0.07	1.75	0.09	−2.82	Na_2O	3.13	3.06	0.11	1.81	0.07	−2.35
K_2O	1.29	1.33	0.05	1.97	0.08	3.22	K_2O	1.96	2.02	0.08	1.86	0.09	3.27
TiO_2	0.70	0.69	0.06	4.49	0.15	−1.45	TiO_2	0.76	0.76	0.08	5.17	0.39	0.40
P_2O_5	0.16	0.14	0.14	51.8	2.78	−17.1	P_2O_5	0.17	0.19	0.08	21.8	1.16	14.3
MnO	0.08	0.02	0.08	234	16.0	−76.3	MnO	0.13	0.15	0.07	21.9	0.96	17.5
Total	99.79	98.87					Total	99.13	99.2712				

NMNH 113716-1	Jarosewich *et al.*,[30] 1980	Mean	2SD	RSD%	2SD	%Bias	NMNH 113498-1	Jarosewich *et al.*,[30] 1980	Mean	2SD	RSD%	2SD	%Bias
SiO_2	51.5	51.1	0.24	0.24	0.01	−0.77	SiO_2	50.9	50.5	0.23	0.23	0.01	−0.78
Al_2O_3	15.4	15.0	0.16	0.88	0.03	−2.21	$FeO_{(t)}$	13.3	13.4	0.16	0.58	0.03	0.95
CaO	11.3	11.2	0.10	0.52	0.03	−0.65	Al_2O_3	12.5	12.3	0.16	0.64	0.03	−1.39
$FeO_{(t)}$	9.13	9.19	0.16	0.44	0.02	0.67	CaO	9.30	9.12	0.11	0.61	0.03	−1.97
MgO	8.21	8.04	0.14	0.86	0.04	−2.07	MgO	5.08	5.05	0.08	0.83	0.04	−0.62
Na_2O	2.48	2.66	0.09	3.62	0.13	7.23	TiO_2	4.06	4.13	0.09	1.07	0.05	1.82
TiO_2	1.30	1.36	0.10	1.62	0.07	4.34	Na_2O	2.66	2.71	0.06	1.13	0.05	2.02
SO_2	0.30	0.27	0.07	14.3	0.73	−9.37	K_2O	0.82	0.87	0.04	2.49	0.14	6.68
MnO	0.17	0.18	0.05	17.0	1.04	8.71	P_2O_5	0.38	0.39	0.08	10.3	0.41	3.79
P_2O_5	0.12	0.08	0.08	44.8	1.67	−30.3	MnO	0.15	0.21	0.06	74.4	4.02	37.9
K_2O	0.09	0.10	0.03	12.1	0.65	7.56	SO_2	0.04	0.04	0.05	62.5	3.21	8.12
Total	100.02	99.29					Total	99.23	98.83				

NMNH VG-2	Jarosewich *et al.*,[30] 1980	Mean	2SD	RSD%	2SD	%Bias	GOR132-G	Jochum *et al.*,[31] 2011	Mean	2SD	RSD%	2SD	%Bias
SiO_2	50.8	50.7	0.26	0.25	0.01	−0.24	SiO_2	45.5	46.0	0.21	0.23	0.01	1.02
Al_2O_3	14.1	13.8	0.11	0.41	0.02	−1.55	MgO	22.4	22.0	0.18	0.42	0.02	−1.94

Table 3 (*Contd.*)

NMNH VG-2	Jarosewich *et al.*,[30] 1980	Mean	2SD	RSD%	2SD	%Bias	GOR132-G	Jochum *et al.*,[31] 2011	Mean	2SD	RSD%	2SD	%Bias
$FeO_{(t)}$	11.8	11.8	0.15	0.63	0.04	−0.57	Al_2O_3	11.0	11.0	0.14	0.62	0.03	0.44
CaO	11.1	10.9	0.11	0.52	0.03	−1.76	$FeO_{(t)}$	10.1	10.2	0.16	0.76	0.03	0.98
MgO	6.95	6.82	0.11	0.82	0.04	−1.84	CaO	8.45	8.48	0.11	0.62	0.03	0.37
Na_2O	2.62	2.69	0.09	1.60	0.06	2.78	Na_2O	0.83	0.86	0.07	4.08	0.21	3.28
TiO_2	1.85	1.89	0.06	1.59	0.08	1.92	Cr_2O_3	0.37	0.40	0.06	7.11	0.35	7.89
SO_2	0.35	0.37	0.08	10.3	0.50	7.21	TiO_2	0.31	0.32	0.05	7.30	0.44	3.92
MnO	0.22	0.21	0.05	10.9	0.74	−3.82	MnO	0.15	0.15	0.12	42.0	2.93	−5.71
P_2O_5	0.20	0.20	0.10	26.0	2.63	−2.40	NiO	0.12	0.14	0.19	66.6	2.35	16.9
K_2O	0.19	0.20	0.04	10.8	0.47	4.63	K_2O	0.03	0.00	0.03	498	75.6	−89.6
Cr_2O_3	0.05	0.00	0.03	498	75.6	−93.6	P_2O_5	0.03					
Cl	0.03	0.00	0.02	498	75.6	−92.0	Total	99.29	99.52				
Total	100.29	99.61											

sample is flat and homogenous. FoV can be set to as low as 1 μm, giving an interaction volume of 5 μm, without noticeable beam damage, this may be optimal for certain applications (*e.g.*, microlite rich scoria). We recommend that for fully quantitative and precise analysis, the FoV is set to 5 μm and the total number of counts is set at 1M counts. Where a smaller field of view is required, we recommend first testing for potential beam damage.

4.3 Data quality

Here, we discuss the accuracy and precision obtained from analysing the suite of ten glass reference materials using the optimal standard acquisition parameters (1M total counts at 5 μm FoV, with an energy of 20 kV and a beam current of 300 pA).

4.3.1 Limit of detection. There is a negative power law relationship between RSD% and element concentration above 0.2 wt%, this relationship breaks down at lower concentrations (Fig. 5). This limit provides an estimate for the limit of detection (LoD) at c. 0.2 oxide wt% using this instrumental set up. Note that the exact value will vary from element to element as a result of differing interferences. SiO_2 and Al_2O_3 are at too high abundance in the nine glasses analysed to resolve their limit of detection. The estimated limit of detection of 0.2 wt% is an order of magnitude higher than can be achieved by EPMA. This represents the one area where EPMA shows a clear advantage over SEM-EDX. EPMA uses WDS, which has detection limits in the 10's of ppm's, and typically operates at a beam current over an order of magnitude that SEM-EDX uses in this study, generating significantly more X-rays, or counts.[47]

4.3.2 Precision. Typical RSD%s for minor elements between 0.2 and 1 oxide wt% range from between 15% and 2.5%, crossing the threshold of 5% at 0.8 oxide wt% (Fig. 5, Tables 3 and ESI 1†). The precision on major elements is typically better than 3 RSD%, decreasing to better than 1 RSD% above 6.5 oxide wt%; similar to the LoD the exact value is element dependent. This analytical precision is comparable to, if not slightly better than, the precision of major element analysis achieved *via* EPMA (*e.g.*, ref. 48 and 49). Analysis on natural glasses spanning a range of compositions thus demonstrate that it is possible to attain highly precise major elements chemistries using SEM-EDX.

4.3.3 Accuracy. All major elements and minor element analyses >0.2 wt% oxide (ESI Table 1†) were compared against the preferred reference values (ref. 30–32, values supplied with

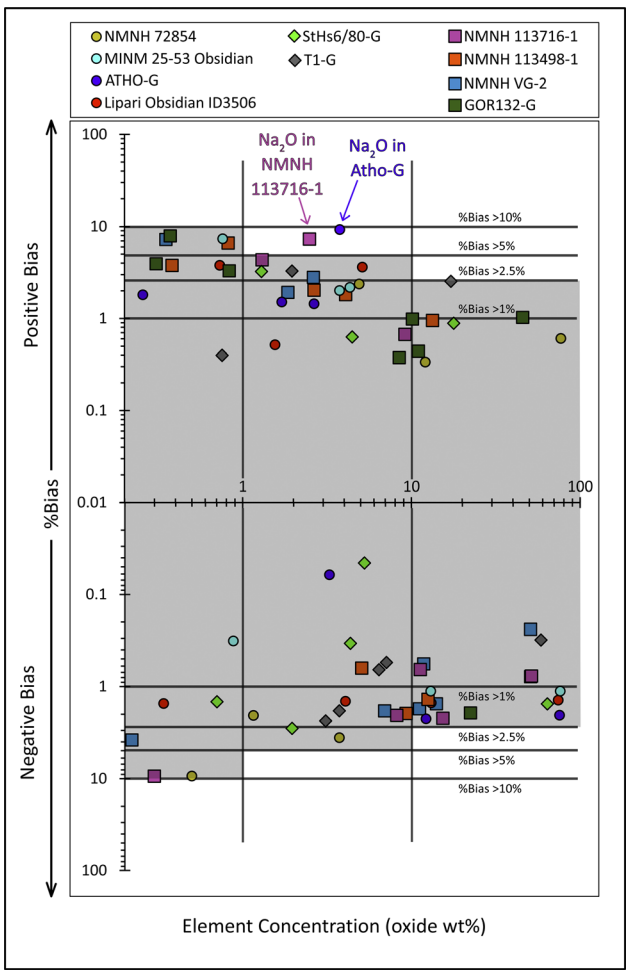

Fig. 6 Spot analysis on a suite of natural glasses (ESI Table 1†) displaying the accuracy using a scanning FoV of 5 μm and for 1M counts. Shaded area outlines analysis within error.

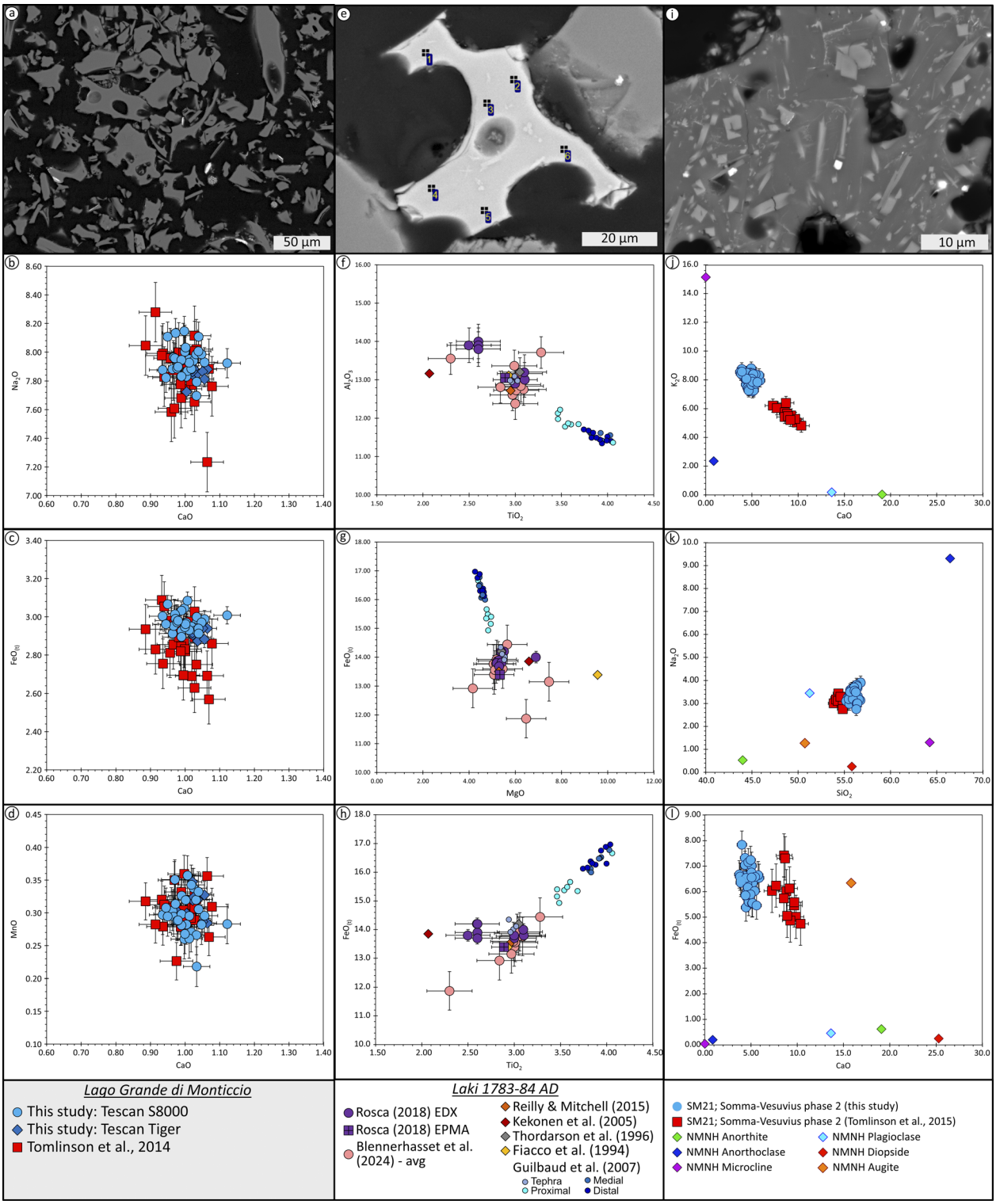

Fig. 7 Panel (a) displays a BSE image of tephra from Lago Grande di Monticchio, Italy. Panels (b–d) show three Harker plots (CaO *vs.* Na_2O, CaO *vs.* FeO(t) and CaO *vs.* MnO) modified from Tomlinson *et al.*, 2014 (ref. 37) with the uncertainty bars showing the standard deviation; These plots compare SEM-EDX analysis on tephra that was produced on two separate SEMs against data produced on the same tephra layer *via* EPMA.[37] Major and minor elements are normalized to 100% and the analytical total given. Panel (e) shows a BSE image of a cryptotephra shard extracted from Brackloon Wood, Co. Mayo, Ireland. Panels (f–h) display scatter plots of Laki 1783-84 AD eruption data with the uncertainty bars showing the standard deviation; TiO_2 *vs.* Al_2O_3, MgO *vs.* FeO(t) and TiO_2 *vs.* FeO(t). EPMA and EDX data from Rosca (2018)[42] and Rosca *et al.* (2019)[40] are outlined in purple. Additional SEM-EDX data from the Laki 1783-84 AD eruption is plotted from Blennerhassett *et al.* (2024).[41] Reilly & Mitchell (2015),[56] Kekonen *et al.* (2005),[51] Thordarson *et al.* (1996)[52] and Fiacco *et al.* (1994)[53] are plotted as additional tephra data. Finally, Icelandic proximal, medial and distal glass from lava selvages and additional tephra data are plotted.[54] Panel (i) displays a BSE image of a microlite-rich volcanic glass from the Pomici di Base eruption of Somma-Vesuvius. Panels (j–l) show Harker plots modified from Tomlinson *et al.* (2015)[39] with

the MINM25-53 Standard Mount) to determine accuracy (expressed as %bias) (Fig. 6, Tables 3 and ESI 1†). Analyses of major elements above 10 wt% are highly accurate, with mean % bias <2.5%. Accuracy on the remaining major elements, aside from Na_2O in NMNH 113716-1 and ATHO-G, is excellent with mean %bias < 5%. All minor elements over 0.20 wt% display mean %bias < 10%. The ATHO-G Na_2O analysis in this study is higher (4.10 ± 0.19 wt%, a %bias of 15.4) than the published preferred content of 3.75 ± 0.31 wt% (Jochum *et al.*, 2006 (ref. 50)). Our analyses are within error of the bulk analyses and ICPMS values of 4.31 ± 0.25 and 4.26 wt% respectively, but higher than the EPMA analyses of 3.53 ± 0.48 wt%. This may reflect Na_2O heterogeneity in the sample, and/or Na_2O loss during EPMA analysis. At the analytical conditions outlined above accuracy is comparable to that achievable *via* EPMA for elements >0.8 wt% abundance. An increase in counts typically results in improvement in accuracy (Table 1).

4.4 Applications

In this section, we show some of the specific advantages offered by SEM-EDX using three case studies of natural sample analyses. One key advantage of SEM-EDX is the faster analysis time and lower cost. Tephrostratigraphic analysis of long lacustrine or marine cores may reveal numerous tephra layers, each of which requires chemical characterization. For example, the composite Largo Grande di Monticchio (LGdM) lacustrine core is 72.5m and contains >300 tephra layers,[36] each requiring 10–30 tephra analyses. Here we analysed LGdM tephra TM-24-3b by SEM-EDX using both the Tescan S8000 and Tescan Tiger SEMs using the optimised conditions (1M counts, 5 μm FoV). Each analysis took approximately 15 seconds, resulting in a significant improvement in total analysis time per tephra layer. Tomlinson *et al.* (2014)[37] acquired major element data on 11 elements using JEOL JXA-8600 electron microprobe, equipped with 4 spectrometers. Count times were 30 s on each peak, except for Na (10 s) and P and Cl (60 s). As shown in Fig. 7a–d, there is good agreement between major and minor element data produced using SEM-EDX (Tiger and S8000) and published EPMA data for the same tephra layer.[37] Analytical totals range from 90.91 to 99.31 wt% (average 95.10 wt%), broadly consistent with the EPMA totals for the same elements (90.50 to 97.7 wt%, average 94.5 wt%). Therefore, accurate and useful tephra data can be acquired major elements using SEM-EDX data. However, larger uncertainties for minor elements (in this example MgO, MnO and Cl) and the inability to detect trace elements (P_2O_5 in this example) preclude the use of these elements for tephra correlation. Nonetheless, SEM-EDX can produce useful tephra data and may be coupled with LA-ICP-MS for analysis of trace elements as is commonly done for EPMA data. All 30 tephra shards analysed on the Tescan S8000 are shown on two BSE images in ESI Fig. 2.† The smallest tephra analysed (TM-24-3b_P15) is approximately 10 μm in diameter, highlighting the spatial resolution of accurate SEM-EDX analysis.

Non-visible tephra layers are known as cryptotephra.[55] These are characterised by low shard concentrations and small shard size (<125 μm by definition, but often much smaller). Cryptotephra extracted from Brackloon Wood, Co. Mayo, Ireland are typically <30 μm in size and are sparse, with only tens of shards per cm^3 of peat.[41] In addition, the vesicular morphologies of many tephra shards mean that the area available for analysis is often much smaller (generally <10 μm in diameter), presenting difficulties for analysis *via* EPMA. Rosca *et al.* (2019)[40] successfully analysed nine cryptotephra shards by SEM-EDX, however was only able to analyse one shard in the same Brackloon mount by EPMA because of the small size of the tephra. SEM-EDX analyses collected at TCD by Rosca *et al.* (2019)[40] and Blennerhassett *et al.* (2024)[41] using the optimised instrumental set up are shown in Fig. 7(e–h). All analyses fall within the range of published data for proximal and distal tephra and lava flows from the Laki 1783-84 AD eruption (ref. 51–54 and 56), indicating that the accuracy and precision of the SEM-EDX data are sufficient for tephra correlations. The use of SEM-EDX thus increases the number of cryptotephra shards that can be analysed and therefore results in more robust tephra correlations.

The spatial resolution advantage of SEM-EDX is further highlighted by analysis of SM21, a scoria rich in feldspar microlites that was produced during the Pomici di Base eruption of Somma-Vesuvius.[38] The microlites are 1–3 μm in diameter and have a spacing of ≤4 μm. Small and closely spaced microlites present a challenge for micron beam analysis as it is difficult to avoid partial overlap with the interaction volume. Accidental analysis of microlites as well as the glass results in smearing of the chemical data towards the composition of the microlite phase(s), thus obscuring the glass composition. This is clearly seen in the EPMA dataset presented by Tomlinson *et al.* (2015),[39] in which the data trend towards higher CaO and lower FeO(t) suggesting partial analysis of the abundant plagioclase and pyroxene microcrystals. For SEM-EDX analysis we used a smaller scanning field of view (1 μm) to avoid interaction with the microlites. The SEM-EDX data are more tightly clustered and provide lower values for of the CaO and higher SiO_2 contents for glass in sample SM21.

5. Conclusions

The data presented show that SEM-EDX can be used to attain highly precise and accurate major element chemistries of glass in a fast and non-destructive manner. Depending on the number of EDX detectors and the pulse processor attached to a SEM, analysis using instrument parameters of 20 kV and 300 pA along with collection of 1M counts should take approximately 15 seconds per spot analysis. Even with one 170 mm^2 Ultim Max EDX detector, analytical time should be less than one

the uncertainty bars showing the standard deviation; CaO *vs.* K_2O, SiO_2 *vs.* Na_2O and CaO *vs.* FeO(t). These plots compare SEM-EDX analysis of the glass from the PdB eruption against data acquired on the same sample using EPMA. Additional published data of six minerals (anorthite, anorthoclase, plagioclase, sanidine, augite and diopside) are plotted.[30] Major and minor elements are normalized to 100% and the analytical total is given. The full dataset for all data in this figure is found in ESI Table 2.†

Table 4 Comparison of SEM-EDX with EPMA

	SEM-EDX	EPMA
Approximate researcher cost per day	$400–500	$700–800
Analysis time for spot analysis for a list of at least 10 elements	≤1 minute	≥3 minutes
Spatial resolution of standard analysis	≤4 μm	>10 μm
Precision (RSD%)	<1 for elements ≥6.5 oxide wt% <3 for the remaining major elements <15 and >2.5 for minor elements	<2 for major elements. <4 for minor elements
Accuracy (%bias)	<2.5% on elements ≥10 oxide wt% <5% on remaining major elements <10% on minor elements ≥0.2 oxide wt%	<2% on major elements
Sodium migration?	No noticeable sodium migration under the above outlined analytical conditions	Sodium depletion is a major issue
Limit of detection?	0.2 oxide wt%	Low ppm range

minute per sample. Chemical data of all elements is collected simultaneously during this time and there is no need to adjust the setup of the instrument during acquisition of spot analyses to account for potential loss of mobile or volatile elements.

Accuracy and precision of major element analyses are comparable to that achieved using EPMA (Table 4). The principal limitation of this technique is that analyses of minor elements are not as precise as can be achieved using EPMA and detection limits are higher at c. 0.2 wt% (using our preferred operational conditions), therefore quantitative analysis of less abundant minor elements and of trace elements requires EPMA or LA-ICP-MS. Fully quantitative SEM-EDX analysis offers advantages of better spatial resolution and faster acquisition time over EPMA and may be the method of choice in studies with a large sample throughput or where the feature of interest is small. Following on from fully quantitative spot analysis, we believe that it should be possible to apply the technique outlined in this study to (a) a diverse range of mineral phases and (b) to acquire fast and accurate SEM-EDX maps, thus expanding the applicability of our approach.

Data availability

The data supporting this article have been included as part of the ESI.†

Conflicts of interest

There are no conflicts to declare.

Acknowledgements

PCG acknowledges support from the Irish Centre for Research in Applied Geosciences (iCRAG) (13/RC/2092-P2). The iCRAG Laboratory at Trinity College Dublin (TCD) was part-funded through a grant to (iCRAG, which is funded under Science Foundation Ireland (SFI) awards (no. 13/RC/2092 and 13/RC/2092-P2). CR acknowledges funding from the People Programme (Marie Currie Actions) IsoNose (www.isonose.eu) of the European Union's Seventhes Framework Programme FP7/2007–2013/under REA grant agreement no [608069]. PCG would like to express thanks to Colin Reid and Leona O'Connor at iCRAB Lab @TCD and Teresa Ubide. CR would like to thank Paul G. Albert and Vicky Cullen for their assistance with the EPMA analyses of the LAKI tephra.

References

1 D. E. Newbury and N. W. Ritchie, Performing elemental microanalysis with high accuracy and high precision by scanning electron microscopy/silicon drift detector energy-dispersive X-ray spectrometry (SEM/SDD-EDS), *J. Mater. Sci.*, 2015, **50**(2), 493–518.
2 V. Lončarić and M. Costa, Known Glass Compositions in Iron Age Europe—Current Synthesis and Emerging Questions, *Heritage*, 2023, **6**(5), 3835–3863.
3 K. V. Cashman and M. Edmonds, Mafic glass compositions: a record of magma storage conditions, mixing and ascent, *Philos. Trans. R. Soc., A*, 2019, **377**(2139), 20180004.
4 R. Li, W. Du and J. Yang, Petrogenesis of the Lunar volcanic glasses and Mg-suite: constraints on a post-magma-ocean cumulate overturn, *Acta Geochim.*, 2022, **41**(4), 717–729.
5 D. J. Lowe and B. V. Alloway. Tephrochronology. in *Encyclopedia of Scientific Dating Methods*. ed. Rink W. J. and Thompson J., Springer Netherlands, Dordrecht, 2013. pp. 1–26.
6 P. M. Abbott and S. M. Davies, Volcanism and the Greenland ice-cores: the tephra record, *Earth-Sci. Rev.*, 2012, **115**(3), 173–191.
7 D. J. Lowe, P. M. Abbott, T. Suzuki and B. J. L. Jensen, Global tephra studies: role and importance of the international tephra research group "Commission on Tephrochronology" in its first 60 years, *Hist. Geo- Space Sci.*, 2022, **13**(2), 93–132.
8 T. Ubide, P. C. Guyett, G. G. Kenny, E. M. O'Sullivan, D. E. Ames, J. A. Petrus, *et al.*, Protracted volcanism after large impacts: Evidence from the Sudbury impact basin, *J. Geophys. Res.: Planets*, 2017, **122**(4), 701–728.
9 S. Kadir, T. Külah, N. Önalgil, H. U. Erkoyun and W. C. Elliott, Mineralogy, Geochemistry, and Genesis of Bentonites in Miocene Volcanic-Sedimentary Units of the

Ankara-Çankiri Basin, Central Anatolia, Turkey, *Clays Clay Miner.*, 2017, **65**, 64–91.

10 A. M. Gueli, S. Pasquale, D. Tanasi, S. Hassam, V. Garro, Q. Lemasson, *et al.*, Non-destructive analyses of Late Roman and Byzantine glasses from ancient Sicily: Methodological challenges and measurable results, *Measurement*, 2018, **129**, 677–685.

11 N. Zacharias, M. Kaparou, A. Oikonomou and Z. Kasztovszky, Mycenaean glass from the Argolid, Peloponnese, Greece: A technological and provenance study, *Microchem. J.*, 2018, **141**, 404–417.

12 J. R. Almirall and T. Trejos, Advanced in the Forensic Analysis of Glass Fragments with a Focus on Refractive Index and Elemental Analysis, *Forensic Sci. Rev.*, 2006, **18**(2), 73–96.

13 M. Ritter, 'Solomon's Bottle': a Glass Bottle in Tehran and Abbasid Glass Floors in Mesopotamia and the Levant, *Journal of Iranian Handicrafts Studies*, 2019, **2**(2), 93–110.

14 V. G. Batanova, A. V. Sobolev and V. Magnin, Trace element analysis by EPMA in geosciences: detection limit, precision and accuracy, *IOP Conf. Ser.: Mater. Sci. Eng.*, 2018, **304**(1), 012001.

15 C. H. Nielsen and H. Sigurdsson, Quantitative methods for electron microprobe analysis of sodium in natural and synthetic glasses, *Am. Mineral.*, 1981, **66**(5–6), 547–552.

16 G. B. Morgan and D. London, Optimizing the electron microprobe analysis of hydrous alkali aluminosilicate glasses, *Am. Mineral.*, 1996, **81**(9–10), 1176–1185.

17 M. C. S. Humphreys, S. L. Kearns and J. D. Blundy, SIMS investigation of electron-beam damage to hydrous, rhyolitic glasses: Implications for melt inclusion analysis, *Am. Mineral.*, 2006, **91**(4), 667–679.

18 E. C. Hughes, B. Buse, S. L. Kearns, J. D. Blundy, G. Kilgour and H. M. Mader, Low analytical totals in EPMA of hydrous silicate glass due to sub-surface charging: Obtaining accurate volatiles by difference, *Chem. Geol.*, 2019, **505**, 48–56.

19 S. L. Kearns, N. Steen and E. Erlund, Electronprobe Microanalysis of Volcanic Glass at Cryogenic Temperatures, *Microsc. Microanal.*, 2002, **8**, 1562–1663.

20 *The Recent Resolution and Detection Limit Improvement of EDS and EBSD with SEM: Invited Paper. 2019 IEEE International Meeting for Future of Electron Devices, Kansai (IMFEDK)*, ed. Morita H., Marks S. and Anderson I., 2019 14-15 Nov. 2019.

21 D. E. Newbury and N. W. M. Ritchie, Elemental mapping of microstructures by scanning electron microscopy-energy dispersive X-ray spectrometry (SEM-EDS): extraordinary advances with the silicon drift detector (SDD), *J. Anal. At. Spectrom.*, 2013, **28**(7), 973–988.

22 V. D. Hodoroaba, S. Rades, T. Salge, J. Mielke, E. Ortel and R. Schmidt, Characterisation of nanoparticles by means of high-resolution SEM/EDS in transmission mode, *IOP Conf. Ser.: Mater. Sci. Eng.*, 2016, **109**(1), 012006.

23 S. Marks, S. Jabar, G. West and S. Burgess, High Resolution Low kV SEM EDS – Breaking Convention with Low Working Distance EDS, *Microsc. Microanal.*, 2020, **26**(S2), 2170–2172.

24 C. G. Pantano Jr, D. B. Dove and G. Y. Onoda Jr, AES compositional profiles of mobile ions in the surface region of glass, *J. Vac. Sci. Technol.*, 1976, **13**(1), 414–418.

25 G. B. Morgan and D. London, Effect of current density on the electron microprobe analysis of alkali aluminosilicate glasses, *Am. Mineral.*, 2005, **90**(7), 1131–1138.

26 D. Chew, K. Drost, J. H. Marsh and J. A. Petrus, LA-ICP-MS imaging in the geosciences and its applications to geochronology, *Chem. Geol.*, 2021, **559**, 119917.

27 X.-H. Li and Q.-L. Li, Major advances in microbeam analytical techniques and their applications in Earth Science, *Sci. Bull.*, 2016, **61**(23), 1785–1787.

28 D. E. Newbury and N. W. M. Ritchie, Is Scanning Electron Microscopy/Energy Dispersive X-ray Spectrometry (SEM/EDS) Quantitative?, *Scanning*, 2013, **35**(3), 141–168.

29 B. Birajdar, N. Peranio and O. Eibl, Quantitative Boron-Analysis Using EDX in SEM and TEM, *Microsc. Microanal.*, 2007, **13**(S03), 290–291.

30 E. Jarosewich, J. A. Nelen and J. A. Norberg, Reference Samples for Electron Microprobe Analysis, *Geostand. Newsl.*, 1980, **4**(1), 43–47.

31 K. P. Jochum, U. Weis, B. Stoll, D. Kuzmin, Q. Yang, I. Raczek, *et al.*, Determination of Reference Values for NIST SRM 610–617 Glasses Following ISO Guidelines, *Geostand. Geoanal. Res.*, 2011, **35**(4), 397–429.

32 S. C. Kuehn, D. G. Froese and P. A. R. Shane, The INTAV intercomparison of electron-beam microanalysis of glass by tephrochronology laboratories: Results and recommendations, *Quat. Int.*, 2011, **246**(1), 19–47.

33 A. Stracke, F. Genske, J. Berndt and J. M. Koornneef, Ubiquitous ultra-depleted domains in Earth's mantle, *Nat. Geosci.*, 2019, **12**(10), 851–855.

34 M. V. Portnyagin, V. V. Ponomareva, E. A. Zelenin, L. I. Bazanova, M. M. Pevzner, A. A. Plechova, *et al.*, TephraKam: geochemical database of glass compositions in tephra and welded tuffs from the Kamchatka volcanic arc (northwestern Pacific), *Earth Syst. Sci. Data*, 2020, **12**(1), 469–486.

35 C. H. Langmuir and G. N. Hanson. Calculating Mineral—Melt Equilibria with Stoichiometry, Mass Balance, and Single-Component Distribution Coefficients, in. *Thermodynamics of Minerals and Melts*, ed. Newton R. C., Navrotsky A. and Wood B. J., Springer New York, New York, NY, 1981, pp. 247–271.

36 S. Wulf, M. Kraml, A. Brauer, J. Keller and J. F. W. Negendank, Tephrochronology of the 100ka lacustrine sediment record of Lago Grande di Monticchio (southern Italy), *Quat. Int.*, 2004, **122**(1), 7–30.

37 E. L. Tomlinson, P. G. Albert, S. Wulf, R. J. Brown, V. C. Smith, J. Keller, *et al.*, Age and geochemistry of tephra layers from Ischia, Italy: constraints from proximal-distal correlations with Lago Grande di Monticchio, *J. Volcanol. Geotherm. Res.*, 2014, **287**, 22–39.

38 A. Bertagnini, P. Landi, M. Rosi and A. Vigliargio, The Pomici di Base plinian eruption of Somma-Vesuvius, *J. Volcanol. Geotherm. Res.*, 1998, **83**(3), 219–239.

39 E. L. Tomlinson, V. C. Smith, P. G. Albert, E. Aydar, L. Civetta, R. Cioni, *et al.*, The major and trace element glass compositions of the productive Mediterranean volcanic sources: tools for correlating distal tephra layers in and around Europe, *Quat. Sci. Rev.*, 2015, **118**, 48–66.

40 C. Rosca, R. Schoenberg, E. L. Tomlinson and B. S. Kamber, Combined zinc-lead isotope and trace-metal assessment of recent atmospheric pollution sources recorded in Irish peatlands, *Sci. Total Environ.*, 2019, **658**, 234–249.

41 L. C. Blennerhassett, P. C. Guyett and E. L. Tomlinson, Tephra identification without pre-separation in ashed peat, *J. Quat. Sci.*, 2024, **39**(5), 816–830.

42 *Peat Bogs as Archives of Atmospheric Metal Pollution from Natural and Anthropogenic Sources - A Case Study from Ireland*, ed. C. Rosca, 2018.

43 A. C. Malti, S. Dembélé, N. Piat, C. Arnoult and N. Marturi, Toward Fast Calibration of Global Drift in Scanning Electron Microscopes with Respect to Time and Magnification, *Int. J. Optomechatronics*, 2012, **6**(1), 1–16.

44 K. Kanaya and S. Okayama, Penetration and energy-loss theory of electrons in solid targets, *J. Phys. D: Appl. Phys.*, 1972, **5**(1), 43.

45 W. V. Mayneord, The significance of the roentgen, *Acta Unio Int. Cancrum*, 1937, **2**, 271–282.

46 M. J. Jercinovic, M. L. Williams, J. Allaz and J. J. Donovan, Trace analysis in EPMA, *IOP Conf. Ser.: Mater. Sci. Eng.*, 2012, **32**(1), 012012.

47 R. S. Frankel and D. W. Aitken, Energy-Dispersive X-Ray Emission Spectroscopy, *Appl. Spectrosc.*, 1970, **24**(6), 557–566.

48 L. Jia, Q. Mao, B. Su, S. Wu, L. Huang, J. Yuan, *et al.*, MK-1 Orthopyroxene—A New Potential Reference Material for In-Situ Microanalysis, *Minerals*, 2021, **11**(12), 1321.

49 L.-H. Jia, Q. Mao, H.-C. Tian, L.-X. Li, L. Qi, S.-T. Wu, *et al.*, High-precision EPMA measurement of trace elements in ilmenite and reference material development, *J. Anal. At. Spectrom.*, 2022, **37**(11), 2351–2361.

50 K. P. Jochum, B. Stoll, K. Herwig, M. Willbold, A. W. Hofmann, M. Amini, *et al.*, MPI-DING reference glasses for in situ microanalysis: New reference values for element concentrations and isotope ratios, *Geochem. Geophys. Geosyst.*, 2006, **7**(2), Q02008.

51 T. Kekonen, J. Moore, P. Perämäki and T. Martma, The Icelandic Laki volcanic tephra layer in the Lomonosovfonna ice core, Svalbard, *Polar Res.*, 2005, **24**(1–2), 33–40.

52 T. Thordarson and S. Self, Sulfur, chlorine and fluorine degassing and atmospheric loading by the Roza eruption, Columbia River Basalt Group, Washington, USA, *J. Volcanol. Geotherm. Res.*, 1996, **74**(1), 49–73.

53 R. J. Fiacco, T. Thordarson, M. S. Germani, S. Self, J. M. Palais, S. Whitlow, *et al.*, Atmospheric Aerosol Loading and Transport Due to the 1783-84 Laki Eruption in Iceland, Interpreted from Ash Particles and Acidity in the GISP2 Ice Core, *Quat. Res.*, 1994, **42**(3), 231–240.

54 M.-N. Guilbaud, S. Blake, T. Thordarson and S. Self, Role of Syn-eruptive Cooling and Degassing on Textures of Lavas from the ad 1783–1784 Laki Eruption, South Iceland, *J. Petrol.*, 2007, **48**(7), 1265–1294.

55 C. S. Lane, V. L. Cullen, D. White, C. W. F. Bramham-Law and V. C. Smith, Cryptotephra as a dating and correlation tool in archaeology, *J. Archaeol. Sci.*, 2014, **42**, 42–50.

56 E. Reilly and F. J. Mitchell, Establishing chronologies for woodland small hollow and mor humus deposits using tephrochronology and radiocarbon dating, *Holocene*, 2015, **25**(2), 241–252.